

Photoelectrochemical water splitting using WO₃ photoanodes: the substrate and temperature roles

Paula Dias,^a Tânia Lopes,^a Laura Meda,^b Luísa Andrade^a and Adélio Mendes^{a,*}

^a LEPABE – Faculdade de Engenharia, Universidade do Porto, rua Dr. Roberto Frias, 4200-465, Portugal.

^b Istituto Guido Donegani per le Energie non Convenzionali, Via Fauser 4, Novara, 28100, Italy.

* E-mail: mendes@fe.up.pt.

The influence of the substrate on the performance of WO₃ photoanodes is assessed as a function of the temperature. Two samples were studied: WO₃ deposited on a FTO glass and anodized on a tungsten foil. Current-voltage curves and electrochemical impedance spectroscopy techniques were used to characterize these samples between 25 °C and 65 °C. The photocurrent-density increased with temperature for both samples and the onset potential shifted to lower potentials. However, for WO₃/FTO, a negative shift of the dark current onset was also observed. The intrinsic resistivity of this substrate limits the photocurrent plateau potential range. On the other hand, this behavior was not observed for WO₃/metal. Therefore, the earlier dark current onset observed for WO₃/FTO was assigned to the FTO layer. The optimal operating temperatures observed were 45 °C and 55 °C for WO₃/FTO and WO₃/metal, respectively. For higher temperatures, the bulk electron-hole recombination phenomenon greatly affects the overall performance of WO₃ photoanodes. The stability behavior was then studied at these temperatures over 72 h. For WO₃/FTO, a crystalline-to-amorphous phase transformation occurred during the stability test, which may justify the current decrease observed after the aging period. The WO₃/metal remained stable, maintaining its morphology and good crystallinity. Interestingly, the preferential orientation of the aged crystals was shifted to the (-222) and (222) planes, suggesting that this was responsible for its better and more stable performance. These findings provide crucial information for allowing further developments on the preparation of WO₃ photoanodes, envisaging their commercial application in PEC water splitting cells.

1. Introduction

The world power consumption is presently about 15 terawatts (TW) and an extra power demand of 10 - 15 TW is envisaged by 2050.^{1,2} To mitigate the effects of this increasing energy demand, the exploitation of renewable energy sources becomes imperative for a sustainable future. The efficient conversion of solar energy into a storable and transportable form of energy is an urgent goal and solar fuels are one viable option.^{3,4} Hydrogen is considered a clean and storable energy carrier if it is produced from renewable energy sources. Photoelectrochemical (PEC) water splitting is a promising process for hydrogen generation from another renewable resource, water, using sunlight as input energy.^{5,6} In fact, PEC cells offer a unique combination of an efficient and low-cost device for producing high purity hydrogen.⁷ The first demonstration of solar water splitting was reported by Fujishima and Honda, in the early 70's, with a TiO₂

semiconductor as photoanode under UV illumination.⁸ The efficiency improvement of solar water splitting based on earth-abundant materials fabricated by scalable processing techniques has continued throughout the years, but only recently attracted worldwide attention.^{6, 9-13}

Photoelectrochemical cells combine the harvesting of solar energy and the water electrolysis in a single device, producing oxygen and hydrogen at physically separated chambers, respectively anode and cathode. The evolved gases can then be collected and stored for a future use. A typical PEC cell consists of a light-absorbing semiconductor electrode (anode) and a metallic counter electrode (cathode), both immersed in an aqueous electrolyte solution; however, the cell can be equipped with two or more photoactive electrodes.^{14, 15} Currently, the selection of the semiconductor electrodes is of great importance in PEC water splitting cells since they have to fulfill several requirements. The electrode materials should have a proper band gap energy (at least 1.9 eV) to cover water dissociation energy (1.23 eV) plus the thermodynamic losses (*ca.* 0.4 eV) and the overpotentials (*ca.* 0.3 eV – 0.4 eV), strong visible light absorption and the band edge positions well positioned to assist oxidation and reduction of water.^{4, 9, 16} Moreover, low-cost, long-term stability in water and under illumination and high energy conversion efficiency are also crucial factors to achieve the required efficiency target of 10 % to enable commercialization.¹⁷

For scaling up this technology it is not only necessary to find new semiconductor materials and to use a versatile PEC cell reactor, but also to understand the behavior of the cell under real outdoor conditions.¹⁸ The performance of the PEC cells should vary essentially as a function of solar irradiance and temperature. Depending on the operating environment (indoor/outdoor applications, geographical location and specific time of the year), temperatures ranging between subzero to near 70 °C can be expected.¹⁹ Despite, only few works have reported the temperature dependence on the PEC cells performance. Mendes *et al.*²⁰ simulated the effect of outdoor conditions (temperature and solar radiation variations) on the energy performance of PEC cells. A linear increase of the current-density with the temperature was observed and the maximum production of hydrogen occurred between 11:00 AM and 1:00 PM (solar time) for undoped hematite photoanodes. Recently, the same group studied the combined effect of temperature variations (from 25 °C to 65 °C) and the aging behavior of a PEC system using Si-doped hematite photoanodes. The results showed a photocurrent density increase with temperature; however, taking into account performance and stability the optimal operation temperature of the PEC cell was *ca.* 45 °C. This study also evidenced that the temperature influences the bare transparent conductive oxide (TCO), which exhibits an earlier dark current onset potential for higher temperatures.²¹

TCO films have been extensively used as a transparent electrode for optoelectronic device applications, *e.g.* for solar cells.^{22, 23} Besides the conductivity and transparency, the main requirements of TCO coatings are the electronic compatibility with adjacent layers in the electrodes and the stability under operating conditions. From the common TCO materials, fluorine doped tin oxide (FTO), indium tin oxide (ITO) and aluminum doped zinc oxide (AZO), only FTO is stable in acidic/alkaline environments.²⁴ In PEC devices, the photoelectrode materials are mostly deposited onto glasses previously covered with a TCO thin layer to assure a transparent photoelectrode. The development of a transparent semiconductor will allow to transmit the fraction of solar radiation not absorbed by the material and to convert it by other

photosystems, improving their overall energy performance. On the other hand, when the transparency is not important, the metal substrate can be a potential alternative for TCO glass substrates. Metal has the advantages of cost-effectiveness, excellent mechanical flexibility and thermal stability in the industrial fabrication processes. Furthermore, metal has high conductivity and good dimensional stability during the processing at elevated temperature.²⁵ The present study aims to evaluate the effect of temperature on the performance of PEC water splitting cells equipped with tungsten trioxide (WO₃) n-type semiconductors. In particular, the main goal of this work is to understand if the photoelectrode substrate plays a critical role on the PEC devices behavior with temperature. Nanostructured WO₃ semiconductor was selected due to its close to optimal bandgap ($E_g = 2.5 - 2.7$ eV) able to capture *ca.* 12 % of the solar spectrum, moderate hole diffusion length (*ca.* 150 nm) and good chemical stability in acidic aqueous solutions under solar illumination, as well as easy and cheap preparation procedures.^{26, 27} The morphology (*e.g.* shape, size and porosity) and crystallinity of WO₃ nanoparticles depend critically on preparation parameters and annealing temperatures, being also limiting factors for PEC cell performance.²⁸⁻³⁰ Herein, the WO₃ photoanodes were prepared using two types of substrates: glass covered with a FTO layer and tungsten metal substrate, *i.e.* WO₃ were deposited by doctor blade on the FTO glass substrate and anodized on a tungsten metal foil. An experimental setup was developed to control the temperature inside the PEC device, allowing its characterization as a function of the temperature. Five temperatures were considered, equally spaced from 25 °C to 65 °C, and the correspondent current-voltage (*J-V*) characteristic curves were obtained in dark and under 1 sun AM 1.5 G illumination (100 mW cm⁻²) conditions. Electrochemical impedance spectroscopy (EIS) measurements were also performed in dark to extract detailed information concerning the charge transfer and accumulation processes occurring in the PEC cell and how they are related to its performance at different temperatures. Aging tests were then conducted for both samples at their best operating temperature during several hours for assessing their stability. Scanning electron microscopy (SEM) and X-ray diffraction (XRD) analysis were carried out to compare the morphology and crystallinity of the WO₃ films under study with the performance of the PEC cell.

2. Experimental

The temperature effect on the performance of water splitting cells using tungsten trioxide photoanodes was studied. The PEC cell was operated from 25 °C to 65 °C with steps of 10 °C. A reference test at 25 °C was always performed between experiments in order to check the photoanode behavior under reference operating conditions. The WO₃ photoanodes were prepared using two types of substrates, FTO glass and tungsten foil; their deposition techniques are described in detail hereafter. The experimental test bench with the PEC cell setup used to control the temperature and the photoelectrochemical measurements are described. Moreover, the stability of these photoanodes was assessed at their best operating temperature (45 °C for WO₃/FTO and 55 °C for WO₃/metal) and their structural and morphological characterization before and after aging tests were also studied.

Photoanode materials preparation

WO₃ photoelectrode on FTO glass substrate (coded hereafter as WO₃/FTO) The WO₃ photoelectrodes were deposited onto FTO (TEC 8, 8 Ω sq⁻¹) glass substrate by the blade-spreading method at Institute ENI Donegani (Novara, Italy), following the procedure named Synt-1, as described elsewhere.³¹ Briefly, tungstic acid was obtained by passing 5 mL of an aqueous Na₂WO₄ solution (10 wt%, Carlo-Erba) through a proton exchange resin (Amberlite IR120H) and the eluted solution was collected in 5 mL of ethanol to slow down the tungstic acid condensation. To the resulting colloidal dispersion, 0.5 g of organic dispersing agent was added and stirred until complete dissolution. WO₃ photoanodes were prepared by blade-spreading the resulting H₂WO₄ colloidal precursor on FTO glass substrates. The resulting films were annealed at 550 °C in air for 2 h.³¹

WO₃ photoelectrode on W metal substrate (coded hereafter as WO₃/metal) The WO₃ photoelectrode on a tungsten foil substrate was prepared by the anodization method at Institute ENI Donegani (Novara, Italy), as described elsewhere.³² The tungsten foil, prior to anodization, was carefully cleaned with acetone and ethanol and sonicated in an Alconox/water solution to remove surface contaminants and oily or greasy impurities. Then, the WO₃ photoanodes were prepared by applying a potential difference of 40 V (Aim-TTi EX752M DC power supply) across the two tungsten foils, which were kept at a distance of about 3 mm. To avoid electrode corrosion, care was taken to reach the final 40 V in about 1 min. This way, a passivation compact oxide was formed during the initial stages of anodization. The total duration of anodization was 5 h in a thermostatic bath at 40 °C.³³

Experimental Setup

To study the temperature effect on the PEC cell performance, an experimental test bench with a temperature controlling system was designed and built, as previously reported by the same group.²¹ Briefly, the electrolyte temperature was controlled using a thermostatic water bath (Julabo model ME, Germany) and the electrolyte pH was monitored using a pH meter (Inolab pH/Cond 740, WTW GmbH, Germany). The PEC cell used has a continuous electrolyte feeding system, described in detail elsewhere.¹⁸ Moreover, a thermocouple was placed inside the cell and a rubber heater was stuck to its back to ensure the desired temperature. Fig. 1 shows the experimental setup used to analyze the behavior of the PEC cell at different temperatures. A standard three-electrode configuration was used with the tungsten trioxide as photoanode, a 99.9 % pure platinum wire (Alfa Aesar, Germany) as counter-electrode and an Ag/AgCl/Sat. KCl (Metrohm, Switzerland) as reference electrode. The cell was filled with an electrolyte aqueous solution of 3 M methanesulfonic acid (25 °C, pH 0.42) in which the photoanode was immersed. The total immersed area of the photoanode was 4 cm².

Photoelectrochemical Characterization

J-V measurements The photocurrent density-voltage (*J-V*) characteristic curves were recorded applying an external potential bias to the cell and measuring the generated photocurrent using a ZENNIUM (Zahner Elektrik, Germany) workstation controlled by the Thales software package (Thales Z 1.0). The potential was reported against the reversible hydrogen electrode (RHE).

The measurements were performed in the dark and under simulated sunlight (Oriel class B solar simulator equipped with a 150 W Xe lamp, Newport, USA), using an AM 1.5 G filter (Newport, USA), at a scan rate of 10 mV s^{-1} for the potential range between $0.3 V_{\text{RHE}}$ and $2.5 V_{\text{RHE}}$. The light beam was calibrated with a single crystal Si photodiode (Newport, USA), resulting in a lamp spectrum that is adjusted to best match the 1 sun spectrum (*ca.* 100 mW cm^{-2}).

EIS measurements Electrochemical impedance spectroscopy (EIS) was performed applying a small potential sinusoidal perturbation to the system and recording the amplitude and the phase shift of the resulting current response using also the ZENNIUM workstation. The frequency range used was $1 \text{ Hz} - 100 \text{ kHz}$ and the magnitude of the modulation signal was 10 mV . The measurements were carried out in dark conditions and at $0.7 V_{\text{RHE}}$, $1.0 V_{\text{RHE}}$, $1.3 V_{\text{RHE}}$ and $1.6 V_{\text{RHE}}$. An appropriate electrical analog was then fitted to the obtained EIS spectra using the ZView software (Scribner Associates Inc., USA).

Aging tests A constant voltage was applied to the PEC cell over several hours and the resulting time-dependent photocurrent response was then measured in order to obtain crucial information about the stability/corrosion of the semiconductor. In this work, the WO_3 photoanodes were continuously exposed to 1 sun AM 1.5 G illumination (100 mW cm^{-2}) over 72 h and at a constant bias potential of $1.23 V_{\text{RHE}}$. The stability was evaluated at their best operating temperature, *i.e.* WO_3/FTO was tested at $45 \text{ }^\circ\text{C}$ and WO_3/metal was tested at $55 \text{ }^\circ\text{C}$.

Structural Characterization

SEM analysis Scanning electron microscopy (SEM) was performed to obtain information about morphology, surface topography and thickness of the WO_3 films in the WO_3/FTO and WO_3/metal samples.

The SEM and EDS analyses were made at CEMUP (Centro de Materiais da Universidade do Porto) using a high-resolution scanning electron microscope (Quanta 400 FEG, FEI Company, USA). The acceleration voltage used was 15 keV while an in-lens detector was employed with a working distance of *ca.* 10 mm . The high resolution images were collected from $2500\times$ up to $200000\times$. The surface of the samples was investigated for fresh and aged samples to assess modifications in their morphology.

XRD analysis X-ray diffraction (XRD) analysis was carried out in a PANalytical X'Pert MPD (Spectris plc, England) equipped with an X'Celerator detector and secondary monochromator ($\text{Cu } K\alpha \lambda = 0.154 \text{ nm}$, 40 kV and 30 mA). The spectra were collected in the range $15^\circ - 95^\circ$ (2 theta) with step size 0.017° and the time acquisition was set to 100 s/step . Rietveld refinement with Powder-Cell software was used to identify the crystallographic phases from the XRD diffraction patterns.

3. Results and Discussion

Temperature effect in PEC cell performance

J-V and EIS measurements were conducted for the two types of WO_3 photoanodes under study, *i.e.* for WO_3 photoanode deposited on FTO glass substrate (WO_3/FTO) and for WO_3 photoanode anodized on a tungsten foil substrate (WO_3/metal). Five different temperatures ($25 \text{ }^\circ\text{C}$, $35 \text{ }^\circ\text{C}$, 45

°C, 55 °C and 65 °C) were considered in dark and under 1 sun AM 1.5 G illumination. Before performing the analysis at each temperature, the cell was left to stabilize for approximately 5 minutes. Fig. 2 a) and b) show the effect of temperature in the J - V characteristics obtained for WO_3/FTO and WO_3/metal samples, respectively

From Fig. 2 is clear that the generated photocurrent density of the PEC cell using WO_3 photoanodes increases with temperature; a similar behavior was also observed with Si-doped hematite photoanodes.²¹ Moreover, the photocurrent density values obtained for WO_3/metal sample is significantly higher than the values obtained for WO_3/FTO sample, being these differences not only due to the preparation methods, but also due to the higher charge transport resistance of the FTO layer in the glass substrate.¹⁸ Actually, the current values obtained are in straight agreement with the ones reported in literature.^{27, 33}

For WO_3/FTO sample, at 25 °C and under dark conditions, the current onset is observed for a potential higher than 2.1 V_{RHE} (the electrolysis threshold for water oxidation with WO_3/FTO photoanodes) – *cf.* Fig. 2 a).³¹ Under sunlight conditions, the photocurrent onset potential begins for 0.5 V_{RHE} and rises steeply up to 1.2 V_{RHE} , reaching a plateau for 1.2 – 2.0 V_{RHE} potential range; a photocurrent density of ca. 0.38 mA cm^{-2} was observed at 1.7 V_{RHE} . After increasing the temperature of the system to 35 °C, a photocurrent density increase of 5 % was achieved at 1.7 V_{RHE} and no significant differences exist between the dark current onset potential at 25 °C and 35 °C. Experiments at higher temperatures were then performed (45 °C, 55 °C and 65 °C) and the same behavior was observed: an improvement of the photocurrent with temperature. In particular, the experiment at 65 °C originated a 64 % photocurrent enhancement at 1.7 V_{RHE} ($J = 0.60 \text{ mA cm}^{-2}$) compared with the experiment performed at 25 °C. However, at this high temperature the dark current onset started at an earlier potential (ca. 1.8 V_{RHE}). Reference tests at 25 °C performed among runs showed only changes in the J - V curves after running the PEC cell at 55 °C and 65 °C; the dark current onset potential was at lower potentials, *i.e.* at 1.9 V_{RHE} and 1.8 V_{RHE} , respectively - see Fig. S1 a) presented in the electronic supplementary information (ESI†).

Regarding the WO_3/metal sample, the highest photocurrent density was also achieved at 65 °C, reaching around 2.01 mA cm^{-2} at 1.23 V_{RHE} and 2.31 mA cm^{-2} at 1.7 V_{RHE} , as shown in Fig. 2 b). Considering 25 °C as the reference temperature, improvements of 114 % and 81%, respectively at 1.23 V_{RHE} and at 1.7 V_{RHE} , were observed. As temperature increases, the onset potential is also shifted to lower potentials, *i.e.* it passed from 0.52 V_{RHE} to 0.40 V_{RHE} , respectively at 25 °C and 65 °C. However, at 65 °C a small current under dark conditions is observed, a behavior that was not observed for temperatures up to 55 °C. Herein, reference tests performed at 25 °C between experiments were also performed and no major changes were observed - see Fig. S1 b) (ESI†).

Analyzing the results presented in Fig. 2, it can be concluded that the photocurrent density increases with temperature and the onset potential shifts to lower potentials, allowing to improve the efficiency of the cell and to reduce the external potential needed to promote the water splitting reaction (bias). Thus, improvements in the PEC cell performance are observed at higher temperatures since temperature contributes to thermal bandgap narrowing of the photoanode (broadening the spectrum range absorption) and also decrease the potential required for the water electrolysis (described by the Nernst equation). Then, a semiconductor operating at higher temperatures will have more available free electrons and holes for charge

transport, an increased intrinsic carrier population and electrolyte conductivity. Finally, mass transport and electroreaction kinetics are also favored by temperature increase, as stated by the Einstein relation and by the Butler-Volmer equation, respectively, outlining a photocurrent improvement with temperature.^{20, 21}

To assess the substrate contribution for the dark current onset potential, J - V characteristic curves for the water hydrolysis were obtained for naked substrates of FTO glass and tungsten foil, as shown in . The hydrogen evolution reaction (HER) is made at a platinum wire cathode and the oxygen evolution reaction (OER) takes place at a FTO glass electrode and at a tungsten foil electrode. For the bare FTO substrate, the dark current onset begins at lower potential values as temperature increases, *e.g.* it begins at $1.9 V_{RHE}$ and $1.4 V_{RHE}$ for temperatures of $25\text{ }^{\circ}\text{C}$ and $65\text{ }^{\circ}\text{C}$, respectively. This behavior is similar to the one obtained for the WO_3/FTO photoanode (Fig. 2).

In typical photoelectrochemical systems the dark current appears at the potential bias when the oxidation/reduction of water occurs. When in contact with an electrolyte in the dark, charge equilibration occurs at the interface, favoring electron/hole recombination. Increasing the temperature, the kinetics is favored due to an increased concentration of free holes in the valence band and so the oxidation of water starts at lower potentials (as outlined by the Nernst equation). For the tungsten foil (metal) substrate this phenomenon is not observed and only a very small anodic dark current density ($< 0.02\text{ mA cm}^{-2}$) was observed as a response to the applied potential bias – Fig. 3.²¹

The inset plot of Fig. 3 shows a detail of the J - V curves for the water hydrolysis at $25\text{ }^{\circ}\text{C}$. It is clearly apparent the difference in the electrochemical activity of both electrodes, being tungsten electrode much less active for OER. For FTO glass substrate the electrocatalytic oxygen evolution starts at *ca.* $1.9 V_{RHE}$, when the dark current sharply increased; for the W substrate a small anodic current density of *ca.* 0.01 mA cm^{-2} is measured up to *ca.* $4.0 V_{RHE}$, when the dark current started to slowly increase. So, the negative shift on the dark current onset as a function of the temperature should be related to the FTO layer and not to the photoanode material.

EIS technique was used to extract detailed information about the group of resistances and capacitances that describe the behavior of the electrochemical reaction kinetics, ohmic conduction processes and mass transport limitations on the PEC cell performance. After obtaining the J - V characteristic curves at the selected temperatures ($25\text{ }^{\circ}\text{C}$, $35\text{ }^{\circ}\text{C}$, $45\text{ }^{\circ}\text{C}$, $55\text{ }^{\circ}\text{C}$ and $65\text{ }^{\circ}\text{C}$), EIS measurements were conducted under dark conditions in a three-electrode configuration. This configuration allows understanding the phenomena occurring at the semiconductor/electrolyte interface, since the potential is measured with respect to a fixed reference potential, short-circuited with the counter-electrode.³⁴ For each operating temperature, a suitable electrical analogue was fitted to the EIS data, as described elsewhere.²¹ The proposed electrical analogue comprises a series resistance (R_{series}) and two RC elements in series representing the semiconductor bulk (R_{sc} and C_{sc}) and the semiconductor/electrolyte interface (R_{ct} and C_H) – Fig. 4. The double layer capacitor does not behave ideally, since the semiconductors are nanostructured and so a constant phase element (CPE) was used instead.³⁴ The impedance tests of the two samples were carried out in the potential range of $0.7 V_{RHE}$ to $1.6 V_{RHE}$, with steps of $0.3 V_{RHE}$; the correspondent Nyquist plots are given in the supplementary

information (ESI+), see Fig. S2 [left plots] and [right plots] for WO₃/FTO and WO₃/metal samples, respectively.

Fig. 5 shows the Nyquist diagrams obtained at 1.6 V_{RHE} for different temperatures; both WO₃ samples exhibit a current plateau at this potential. The overall resistance ($R_{series} + R_{SC} + R_{CT}$) decreases with temperature for both WO₃ samples, in line with the photocurrent density evolution; however, the overall PEC cell resistance is higher for WO₃/FTO sample. By zooming the Nyquist diagram at the high frequency range, it is observed that a temperature independent small semicircle appears for the WO₃/FTO sample [inset plot in Fig. 5 a)], which is imperceptible in the WO₃/metal sample [inset plot in Fig. 5 b)]. The latter is assigned to FTO exposure to the electrolyte; this new interface (FTO/electrolyte interface) imposes an extra resistance to the system (not considered in the proposed model).

Fitting the electrical circuit analogue shown in Fig. 4 to experimental EIS data, the impedance parameters such as R_{series} , R_{SC} , C_{SC} , R_{CT} and C_H were then obtained. The EIS spectra obtained at the high frequency range, assigned to the faster electronic processes occurring in the semiconductor bulk, was fitted to the RC element composed of R_{SC} and C_{SC} , whereas the low frequency range spectra, assigned to the phenomena occurring at the semiconductor/electrolyte interface, was fitted to R_{CT} and C_H . In fact, the temperature increase strongly affects the phenomena occurring at the semiconductor/electrolyte interface, since the low frequencies range semicircle decreases considerably with temperature, being this decrease even more obvious at higher temperatures (65 °C). The obtained parameters are plotted in Fig. 6 as a function of the temperature for 1.6 V_{RHE}.

Fig. 6 shows the differences between the impedance parameter values for the two photoanodes under study. The series resistances, R_{series} , for the WO₃/FTO sample are considerable higher than the ones for the WO₃/metal sample, as shown in Fig. 6 a). Additionally, R_{series} for WO₃/FTO sample decreases from 8.0 Ω to 5.1 Ω when the temperature increases from 25 °C to 65 °C. This behavior is not observed for the WO₃/metal sample, remaining the R_{series} values almost constant (ca. 0.4 Ω) for the studied temperatures. The series resistance comprehends the substrate resistance, the resistance related to the electrolyte ion conductivity and the resistance of the external contacts (e.g. wire connections).³⁵ It can then be concluded that the main contribution to the R_{series} is the substrate resistance to the transport of charges, since the other series resistances are equal for both electrodes. FTO layer imposes a higher resistance and, consequently, decreases the charge collection efficiency in the external circuit.

The electrical resistance related to the bulk semiconductor, R_{SC} , should decrease with temperature, associated to a faster electron transport through the WO₃ photoactive material.²¹ For the WO₃/metal sample, R_{SC} decreases from 6.9×10^2 Ω to 1.3×10^2 Ω when temperature increases from 25 °C to 65 °C and a more pronounced decrease is observed at 55 °C - cf. Fig. 6 b). Fig. 6 c) shows the behavior of the charge transfer resistance, R_{CT} , and a decrease with temperature is observed for both samples; so no differences related to the temperature effect in the resistance contribution on the substrate material are noticed. The major differences are related to the electrocatalytic activity of the WO₃ semiconductor material³⁶; in the temperature range studied, R_{CT} decreased from 3.4×10^3 Ω to 3.9×10^2 Ω and 7.5×10^4 Ω to 1.2×10^4 Ω for the WO₃/metal and WO₃/FTO samples, respectively. Moreover, the R_{CT} decrease with temperature is responsible by an enhanced charge transfer phenomena. If the overall resistance

in the system favors the photocurrent increase with temperature, this means that the R_{CT} decrease has a more pronounced effect than the R_{SC} decrease.

On the other hand, the space charge capacitance (C_{SC}) and the Helmholtz capacitance (C_H) are almost temperature independent – cf. Fig. 6 d) and e), respectively. The C_H values are higher than the C_{SC} values, since the Helmholtz double layer width is generally smaller than the width of the depletion layer in photo-assisted water splitting systems.²¹

Fig. 6 f) shows the evolution of the rate constant (k_r) of the bulk electrons recombination with holes in the space charge layer as a function of the operating temperature. It corresponds to the inverse of the time constant of the bulk semiconductor RC element (obtained by multiplying the semiconductor resistance, R_{SC} , with the correspondent capacitance, C_{SC}). The recombination rate constant is in the range of $100 - 1 \text{ s}^{-1}$ and a faster electron-hole recombination (higher k_r) is observed with temperature for both samples. This process is ascribed to an increased back electron reaction promoted by accumulated charges on the surface of the photoanode, resulting in higher surface recombination. The recombination loss pathway has to be taken into account for the performance of PEC cells, since it is potentially in direct kinetic competition with water oxidation. In particular, the recombination rate constant strongly increases at 55 °C and 65 °C for WO_3/FTO sample and at 65 °C for WO_3/metal sample. The intrinsic power characteristics of the WO_3 photoelectrodes were obtained from the J - V curves (Fig. 2) as a function of the temperature: power conversion (P) efficiency, fill factor (FF), intrinsic solar to chemical ($ISTC$) conversion efficiency of the photoanode, photocurrent density (J_{photo}) and correspondent photovoltage (V_{photo}). These parameters were determined following the work reported by Rothschild *et al.*³⁷. The intrinsic photovoltaic power of the photoanodes is the product of photocurrent by photovoltage; by plotting it versus photovoltage, the maximum power point (MPP) can be obtained and the respective voltage (V_{MPP}) and current (J_{MPP}). The $ISTC$ efficiency was determined from the following equation:

$$ISTC = \eta_{el} \frac{J_{\text{photo}} \times V_{\text{photo}}}{P_{\text{light}}} \Big|_{\text{AM1.5G}} \quad (1)$$

$$\cong \frac{1.23 \text{ (VRHE)}}{U_{\text{dark}} \text{ (VRHE)}} \left[\frac{J_{\text{photo}} \text{ (mA cm}^2\text{)} \times V_{\text{photo}} \text{ (V)}}{100 \text{ (mW cm}^2\text{)}} \right]$$

where η_{el} is the electrolysis efficiency and U_{dark} is the dark current. The temperature effect in the intrinsic power characteristics of WO_3/FTO and WO_3/metal samples is shown in Fig. 7; the summary of the parameters at the maximum power point is also presented in Table S1 (ESI†).

Fig. 7 shows that maximum power and intrinsic solar to chemical conversion efficiencies increase with temperature for both types of WO_3 photoanodes, being the obtained values higher for the WO_3/metal sample, as expected from the J - V characteristics. However, the fill factor parameter for the WO_3/FTO sample increases only until 45 °C (see Table S1 - ESI†). This can be explained by the enhanced charge recombination loss for temperatures higher than 45 °C, since a reduction of FF is normally reached when the recombination rate is significantly higher than the extraction rate.³⁸ Actually this was validated by EIS measurements (Fig. 6), where the recombination rate constant of the bulk electrons with holes strongly increases for the two higher temperatures. The results indicated that the trend of each intrinsic power parameters depends on the

recombination rate constant, which is also affected by the temperature and the semiconductor interfaces present in the solar cell.³⁹ Therefore, a PEC device equipped with the WO₃/FTO photoanode showed the optimal performance conditions when operating at 45 °C, ensuring simultaneously the highest fill factor, $FF = 72.69\%$, a power conversion, P , value of *ca.* 0.57 mW·cm⁻² and an intrinsic solar to chemical conversion, $ISTC$, efficiency value of *ca.* 0.28 %. Regarding the cell using the WO₃/metal sample, even if the best performance was observed at 65 °C ($FF = 50.84\%$, $P = 2.20\text{ mW}\cdot\text{cm}^{-2}$ and $ISTC = 2.38\%$) the improvement in terms of FF is only *ca.* 0.55 % due to a noticeable increase of the k_r value [Fig. 6 f)]. Balancing this behavior with an increased dark current at 65 °C (Fig. 2), the best operating temperature should be considered at 55 °C.

Stability behavior of PEC cell at high temperatures

The performance histories of the WO₃/FTO and WO₃/metal samples were evaluated at the best operating temperature abovementioned, 45 °C for WO₃/FTO and 55 °C for WO₃/metal sample. A reference stability test was also performed at room temperature (25 °C) with a fresh WO₃/FTO sample. Fig. 8 plots the photocurrent histories over 72 hours under continuous 1 sun AM 1.5 G illumination for both samples.

From Fig. 8 significant photocurrent density decrease is observed during the initial period of 4 hours for both samples, which is typical for the WO₃ photoanodes, as reported elsewhere.^{26, 27} Photocurrent remains mostly stable over 60 hours (after the initial period) for the WO₃/FTO photoanode with an average value of 0.51 mA cm⁻² and 0.57 mA cm⁻² for samples aged at 25 °C and 45 °C, respectively. The test was stopped after 72 hours, when the photocurrent of both samples lost approximately 10 %. Since the reference stability test at 25 °C and the test at 45 °C showed similar behaviors, it can be concluded that temperature increase up to 45 °C allows to improve the efficiency of the PEC cell with no significant influence on the stability performance. The J - V characteristics of both samples before and after running the stability tests at 25 °C and 45 °C are shown in Fig. S3 (ESI[†]). Under simulated sunlight conditions and at 25 °C, the photocurrent at 1.23 V_{RHE} decreased after the stability test from *ca.* 0.56 mA cm⁻² to 0.47 mA cm⁻²; likewise, at 45 °C it decreased from *ca.* 0.66 mA cm⁻² to 0.53 mA cm⁻². In dark conditions, the onset potential for both samples tends to appear at lower potentials after aging, *i.e.* moved from 2.1 V_{RHE} to 2.0 V_{RHE}. The dark current onset at lower potentials may be related to semiconductor detachment from the substrate, allowing FTO areas to contact directly with the electrolyte. The morphology of the WO₃/FTO film was then investigated by SEM and EDS before and after performing the stability tests to assess the surface integrity of the samples - Fig. 9. Before the aging test, SEM images of the WO₃/FTO sample show a network of plate-like particles with diameters of a few tens of nanometers (ranging from 20 to 50 nm) partly fused together, forming a WO₃ nanocrystalline film of *ca.* 1.1 μm thick – *cf.* Fig. 9 a).²⁸ The EDS analysis of area Z1 in Fig. 9 a) (3) displays just the presence of tungsten (W) and oxygen (O) elements. Fig. 9 b) (4) and c) (7) show similar film morphology for WO₃/FTO samples after performing the stability tests at 25 °C and 45 °C, respectively. The aged WO₃ surfaces seem to present higher porosity assigned to material detachment from the FTO glass substrate. Fig. 9 b) (5) shows two distinct areas in the sample aged at 25 °C: area Z1 that apparently was unaffected by corrosion and area Z2 affected by film degradation. In the sample aged at 45 °C it can be detected three

different areas: an intact area (Z1) and two degraded areas (Z2 and Z3) – *cf.* Fig. 9 c) (8). For both aged samples, the EDS analysis confirmed the presence of tin (Sn) in the areas potentially affected by corrosion; these results are in agreement with other studies.^{21, 35} Since the samples aged at 25 °C and 45 °C show similar morphologic degradation, it can be concluded that the photocurrent loss should not be ascribed to the temperature effect.

Concerning the stability performance of the WO₃/metal sample evaluated at 55 °C, after a photocurrent decrease of *ca.* 9 % during the initial 4 hours, the generated photocurrent density remained almost stable for whole period of 72 hours [Fig. 8 b)]. Thus, a current value of *ca.* 1.47 mA cm⁻² was reached at the end, corresponding to *ca.* 2 % decrease after the initial period. From the *J-V* characteristics, no significant differences in the dark current were observed before and after running the aged tests, as shown in Fig. S3 (ESI+). Fig. 10 shows SEM images of the fresh and aged WO₃/metal sample. The fresh sample presents the typical “crispy” surface composed of nanoparticles (*ca.* 50 - 100 nm) interconnected by a nanoscopic structure with an average layer thickness of *ca.* 3.5 μm.³³ This consists of a two-layers nanostructure: a compact oxide layer of *ca.* 1.3 μm originated by the first anodization of the starting tungsten foil, followed by a porous nanoparticle oxide layer of *ca.* 2.2 μm – *cf.* Fig. 10 a) (2). No morphologic changes were observed on the aged sample. Moreover, EDS analysis of both samples only detected W and O elements – *cf.* Fig. 10 (3) and (6).

The crystallinity of the WO₃ films also influences the efficiency and stability of the PEC water splitting cells, since the number of grain boundaries and recombination centers associated with the degree of photoelectrode crystallinity control the photoelectrochemical properties of the films.^{28, 40} In this regard, XRD patterns of the WO₃ films before and after aging tests were obtained and are presented in Fig. 11.

For WO₃/FTO samples [Fig. 11 a)], the reflection peaks of the fresh sample (blue line) completely matches with WO₃ monoclinic phase (JCPDS 01-083-0950); a series of peaks (labeled with asterisk) originated from the dense F:SnO₂ layer (FTO) (cassiterite), underneath the semiconductor layer, are also detected. The XRD spectrum of a preferentially orientated monoclinic WO₃ film exhibits the characteristic triplet for peaks at 23.1°, 23.6° and 24.4°, corresponding to (002), (020) and (200) planes; peaks at range 33° - 35° and 41° - 42° are also presented but with less intensity. This sample shows a high intensity peak at 2 theta = 24.4°, indicating a (200) preferential orientation of the WO₃ crystallites parallel to the FTO glass substrate. However, the aged WO₃/FTO sample (red line) showed an amorphous structure. This should contribute to the photocurrent decrease after 60 h, since it is known that improved crystallinity is advantageous to the photoelectrode performance, ascribed to the decreased number of recombination sites.⁴⁰

On the other hand, for fresh and aged WO₃/metal sample, the diffraction patterns indicate the presence of a crystalline monolithic phase – *cf.* Fig. 11 b). Again, the WO₃ patterns are superimposed on the metallic tungsten substrate pattern. Before testing (blue line), the WO₃/metal film presented a (020) preferential orientation, although the double peak around 41.6°, representing the (-222) and (222) planes, is also strong. Despite the WO₃ films for WO₃/FTO and WO₃/metal samples were both monoclinic phase, they had different preferential orientation of crystal faces. This can be related to different fabrication methods as well as different film adhesion to the substrate that should be accounted for the photocurrent and

stability performance of the semiconductor materials. After aging tests (red line), the double peak at 41.6° was the mainly detected, indicating the preferential orientation of the aged WO_3 crystal faces to the (-222) and (222) planes. Interestingly, the presence of this double peak with an intensity order similar to the fresh sample can justify the high stability performance of the WO_3 photoanodes anodized on tungsten foil substrates. Hence, the relatively good crystallinity of this sample and the preservation of morphology contributed to its highest PEC performance for oxygen evolution reaction. The optimal operation temperature for WO_3/metal photoanode is then *ca.* 55°C , since it ensures simultaneously the highest photocurrent density and stable performance.

4. Conclusions

The temperature influence on the PEC cell performance using WO_3 photoanodes for water splitting was studied. The WO_3 photoanodes were prepared on different substrates by using two techniques: deposition by blade spreading method on a FTO glass substrate and anodization of a tungsten foil substrate. Herein, the main goal was the assessment of the substrate type role on the photoelectrode performance as a function of the temperature. *J-V* characteristic curves, EIS measurements and aging tests were used, as well as SEM and XRD analysis, to assess the morphology and crystallography of the prepared WO_3 samples.

The PEC device was characterized from 25°C to 65°C , with steps of 10°C . At 25°C , the highest photocurrent density was reached for the WO_3/metal photoanode, *ca.* 0.94 mA cm^{-2} at $1.23\text{ V}_{\text{RHE}}$, whereas a photocurrent of *ca.* 0.36 mA cm^{-2} was obtained for the WO_3/FTO sample. These differences are not only due to the semiconductor preparation method but also to the much higher charge transport resistance imposed by the FTO substrate. When the temperature is further increased to 45°C , the generated photocurrent increased *ca.* 20 % in the case of the WO_3/FTO sample and *ca.* 29 % for the WO_3/metal sample, both at $1.23\text{ V}_{\text{RHE}}$. At the maximum tested temperature (65°C) both samples generated higher photocurrents at $1.23\text{ V}_{\text{RHE}}$, *i.e.* 2.02 mA cm^{-2} and 0.62 mA cm^{-2} for the WO_3 on FTO and metal substrates, respectively. However, the WO_3/metal showed a small current under dark conditions, while the WO_3/FTO exhibited already a quite high dark current onset potential at *ca.* $1.80\text{ V}_{\text{RHE}}$. The negative shift on the dark current onset potential of the WO_3/FTO was mainly attributed to temperature effect on FTO glass substrate and not to the photoanode material.

The *J-V* and impedance measurements allowed concluding about the optimal operating temperature for each photoelectrode type: 45°C for the WO_3/FTO sample and 55°C and the WO_3/metal sample. For higher temperatures, an increased recombination rate of the bulk electrons with holes was observed, which is in direct kinetic competition with water oxidation and, consequently, should affect the overall performance of the photoanodes. The aging tests performed at these temperatures showed that WO_3/metal has simultaneously the best stability and performance for the oxygen evolution reaction. No degradation was observed for aged WO_3/metal film; this behavior might be related to the preferential orientation of the crystal faces – (-222) and (222) planes. WO_3/FTO exhibited a slight photocurrent decrease after aging for both temperatures tested (25°C and 45°C). The performance loss was attributed to changes in the monoclinic crystalline structure of the WO_3/FTO film, *i.e.* the semiconductor layer became

amorphous. Therefore, the substrate and application method have a significant role on the photoelectrode energy performance and stability.

Acknowledgements

P. Dias and T. Lopes are grateful to the Portuguese Foundation for Science and Technology (FCT) for their PhD fellows (references: SFRH/BD/81016/2011 and SFRH/BD/62201/2009, respectively). L. Andrade acknowledges European Research Council (ERC) for funding within project BI-DSC – Building Integrated Dye sensitized Solar Cells (contract number: 321315). This work was financially supported by: Project UID/EQU/00511/2013-LEPABE (Laboratory for Process Engineering, Environment, Biotechnology and Energy – EQU/00511) by FEDER funds through Programa Operacional Competitividade e Internacionalização – COMPETE2020 and by national funds through FCT (Project H2Solar; reference PTDC/EQU-EQU/104217/2008). Financial support by the ERC (Project NanoPEC - Nanostructured Photoelectrodes for Energy Conversion; contract number: 227179) is also acknowledged. The authors would like to acknowledge the fruitful discussions with Dr. C. Mateos and Dr. P. Tavares concerning the XRD analysis. The authors are also thankful to CEMUP for the SEM/EDS analysis.

References

1. BP Statistical Review of World Energy 2015, <http://www.bp.com/en/global/corporate/energy-economics/statistical-review-of-world-energy.html>).
2. R. Krol, eds. R. van de Krol and M. Grätzel, Springer US, 2012, vol. 102, pp. 3-12.
3. B. A. Pinaud, J. D. Benck, L. C. Seitz, A. J. Forman, Z. Chen, T. G. Deutsch, B. D. James, K. N. Baum, G. N. Baum, S. Ardo, H. Wang, E. Miller and T. F. Jaramillo, *Energy & Environmental Science*, 2013, **6**, 1983-2002.
4. M. G. Walter, E. L. Warren, J. R. McKone, S. W. Boettcher, Q. Mi, E. A. Santori and N. S. Lewis, *Chemical Reviews*, 2010, **110**, 6446-6473.
5. M. Z. Jacobson, *Energy & Environmental Science*, 2009, **2**, 148-173.
6. M. Grätzel, *Nature*, 2001, **414**, 338-344.
7. R. Krol, eds. R. van de Krol and M. Grätzel, Springer US, 2012, vol. 102, pp. 13-67.
8. A. Fujishima and K. Honda, *Nature*, 1972, **238**, 37-38.
9. R. Krol, Y. Liang and J. Schoonman, *Journal of Materials Chemistry*, 2008, **18**, 2311-2320.
10. R. Abe, *Journal of Photochemistry and Photobiology C: Photochemistry Reviews*, 2010, **11**, 179-209.
11. J. Azevedo, L. Steier, P. Dias, M. Stefik, C. T. Sousa, J. P. Araujo, A. Mendes, M. Graetzel and S. D. Tilley, *Energy & Environmental Science*, 2014, **7**, 4044-4052.
12. T. Hisatomi, J. Kubota and K. Domen, *Chemical Society Reviews*, 2014, DOI: 10.1039/C3CS60378D.
13. N. S. Lewis and D. G. Nocera, *Proc. Natl. Acad. Sci. U.S.A.*, 2006, **103**, 15729.
14. L. Andrade, T. Lopes, H. A. Ribeiro and A. Mendes, *International Journal of Hydrogen Energy*, 2011, **36**, 175-188.
15. T. Lopes, P. Dias, L. Andrade and A. Mendes, *Energy Procedia*, 2012, **22**, 35-40.

16. P. Dias, M. Schreier, S. D. Tilley, J. Luo, J. Azevedo, L. Andrade, D. Bi, A. Hagfeldt, A. Mendes, M. Grätzel and M. T. Mayer, *Advanced Energy Materials*, 2015, DOI: 10.1002/aenm.201501537, n/a-n/a.
17. J. W. Ager III, M. Shaner, K. Walczak, I. D. Sharp and S. Ardo, *Energy & Environmental Science*, 2015, DOI: 10.1039/C5EE00457H.
18. T. Lopes, P. Dias, L. Andrade and A. Mendes, *Solar Energy Materials and Solar Cells*, 2014, **128**, 399-410.
19. S. Haussener, S. Hu, C. Xiang, A. Z. Weber and N. S. Lewis, *Energy & Environmental Science*, 2013, **6**, 3605-3618.
20. L. Andrade, T. Lopes and A. Mendes, *Energy Procedia*, 2012, **22**, 23-34.
21. P. Dias, T. Lopes, L. Andrade and A. Mendes, *Journal of Power Sources*, 2014, **272**, 567-580.
22. C. Guillén and J. Herrero, *Thin Solid Films*, 2011, **520**, 1-17.
23. C. G. Granqvist, *Solar Energy Materials and Solar Cells*, 2007, **91**, 1529-1598.
24. M. Stefik, M. Cornuz, N. Mathews, T. Hisatomi, S. Mhaisalkar and M. Grätzel, *Nano Letters*, 2012, **12**, 5431-5435.
25. V. Kumar and H. Wang, *Solar Energy Materials and Solar Cells*, 2013, **113**, 179-185.
26. R. Solarska, R. Jurczakowski and J. Augustynski, *Nanoscale*, 2012, **4**.
27. H. Qi, J. Wolfe, D. Wang, H. J. Fan, D. Fichou and Z. Chen, *Nanoscale*, 2014, **6**, 13457-13462.
28. C. Santato, M. Odziemkowski, M. Ulmann and J. Augustynski, *Journal of the American Chemical Society*, 2001, **123**, 10639-10649.
29. X. Liu, F. Wang and Q. Wang, *Physical Chemistry Chemical Physics*, 2012, **14**, 7894-7911.
30. T. Zhu, M. N. Chong and E. S. Chan, *ChemSusChem*, 2014, **7**, 2974-2997.
31. L. Meda, G. Tozzola, A. Tacca, G. Marra, S. Caramori, V. Cristino and C. Alberto Bignozzi, *Solar Energy Materials and Solar Cells*, 2010, **94**, 788-796.
32. L. Meda, A. Tacca, C. A. Bignozzi, S. Caramori and V. Cristino, *Journal*, 2012.
33. A. Tacca, L. Meda, G. Marra, A. Savoini, S. Caramori, V. Cristino, C. A. Bignozzi, V. G. Pedro, P. P. Boix, S. Gimenez and J. Bisquert, *ChemPhysChem*, 2012, **13**, 3025-3034.
34. T. Lopes, Andrade, L., and Mendes, A., in *Solar Energy Sciences and Engineering Applications*, ed. A. A. Napoleon Enteria, CRC Press Taylor & Francis Group, 2013, ch. 10, p. 692.
35. T. Lopes, L. Andrade, F. Le Formal, M. Gratzel, K. Sivula and A. Mendes, *Physical Chemistry Chemical Physics*, 2014, DOI: 10.1039/C3CP55473B, 16515-16523.
36. C. A. Bignozzi, S. Caramori, V. Cristino, R. Argazzi, L. Meda and A. Tacca, *Chemical Society Reviews*, 2013, **43**, 2228.
37. H. Dotan, N. Mathews, T. Hisatomi, M. Grätzel and A. Rothschild, *The Journal of Physical Chemistry Letters*, 2014, **5**, 3330-3334.
38. D. Bartesaghi, I. d. C. Perez, J. Kniepert, S. Roland, M. Turbiez, D. Neher and L. J. A. Koster, *Nat Commun*, 2015, **6**.
39. J. Macaira, I. Mesquita, L. Andrade and A. Mendes, *Physical Chemistry Chemical Physics*, 2015, **17**, 22699-22710.
40. C. Ng, Y. H. Ng, A. Iwase and R. Amal, *ACS Applied Materials & Interfaces*, 2013, **5**, 5269-5275.

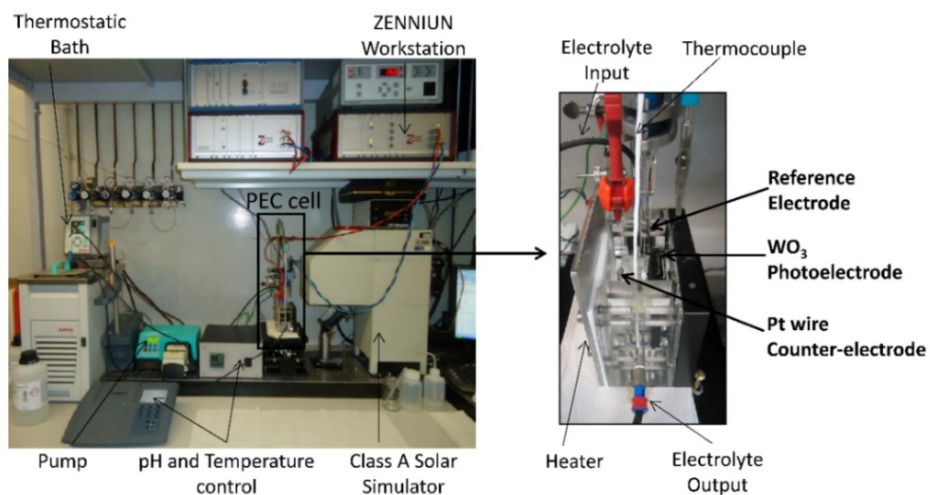


Fig. 1 Test bench setup used to characterize the PEC cell at different temperatures.

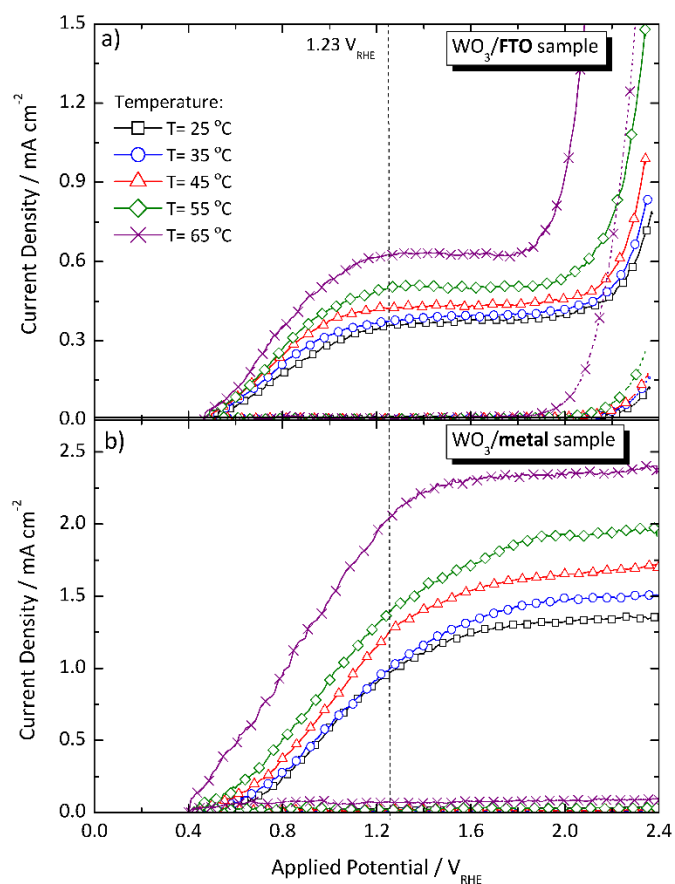


Fig. 2 Temperature effect in the photocurrent density-voltage ($J-V$) characteristics of the WO_3 photoanodes: a) WO_3/FTO sample and b) WO_3/metal sample; for a range of temperatures from 25 °C to 65 °C, in the dark (dashed lines) and under 1 sun AM 1.5 G illumination (solid lines). (\square) $T = 25$ °C, (\circ) $T = 35$ °C, (Δ) $T = 45$ °C, (\diamond) $T = 55$ °C, (\times) $T = 65$ °C.

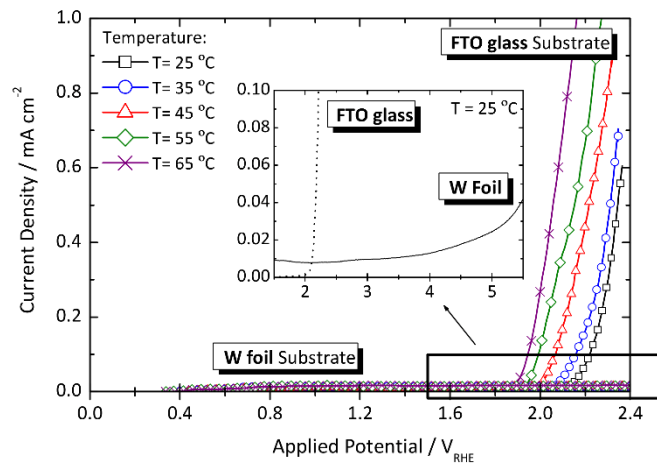


Fig. 3 Temperature effect in the photocurrent density-voltage (J - V) characteristics of a bare FTO-glass and a metal (tungsten foil) substrates for a range of temperatures from 25 °C to 65 °C in the dark conditions. (\square) $T = 25$ °C, (\circ) $T = 35$ °C, (\triangle) $T = 45$ °C, (\diamond) $T = 55$ °C, (\times) $T = 65$ °C.

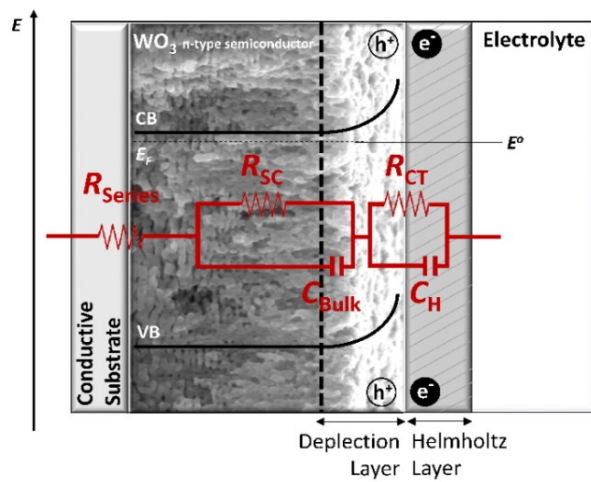


Fig. 4 Electrical circuit analog used to fit the EIS data.

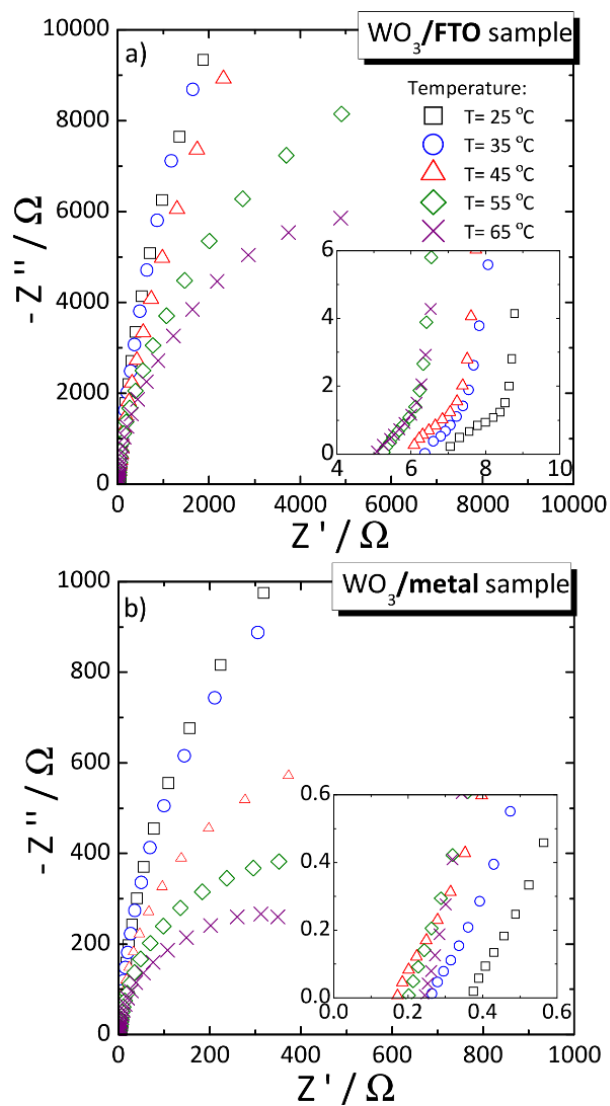


Fig. 5 Temperature effect in the Nyquist diagrams of the WO_3 photoanodes: a) WO_3/FTO sample and b) WO_3/metal sample; for a range of temperatures from 25°C to 65°C , obtained in dark by applying a potential of $1.6 \text{ V}_{\text{RHE}}$. Z' : real impedance, Z'' : imaginary impedance; (\square) $T = 25^\circ\text{C}$, (\circ) $T = 35^\circ\text{C}$, (\triangle) $T = 45^\circ\text{C}$, (\diamond) $T = 55^\circ\text{C}$, (\times) $T = 65^\circ\text{C}$. On the right corner of each plot is a zoom-out of the plots.

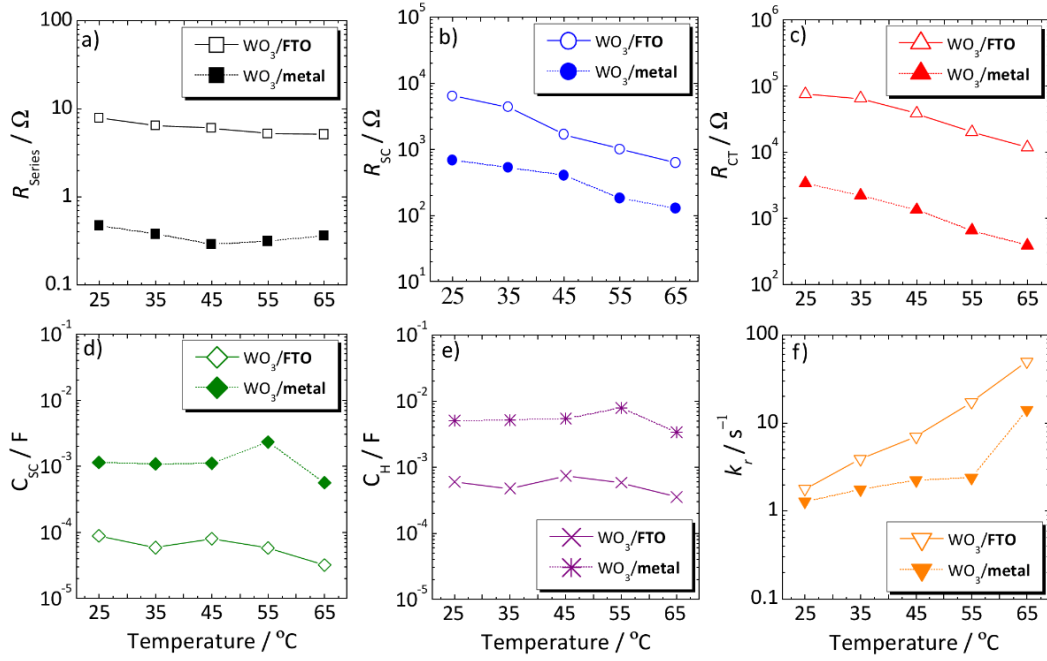


Fig. 6 Temperature effect in the impedance parameters for WO_3/FTO sample (empty symbols) and WO_3/metal sample (filled symbols) obtained at 1.6 V_{RHE} : a) series resistance - R_{S} (\square), b) bulk semiconductor resistance - R_{SC} (\circ), c) charge transfer resistance - R_{CT} (Δ), d) space charge capacitance - C_{SC} (\diamond), e) Helmholtz capacitance - C_{H} (\times), f) rate constant of the electron-hole recombination - k_{r} (∇).

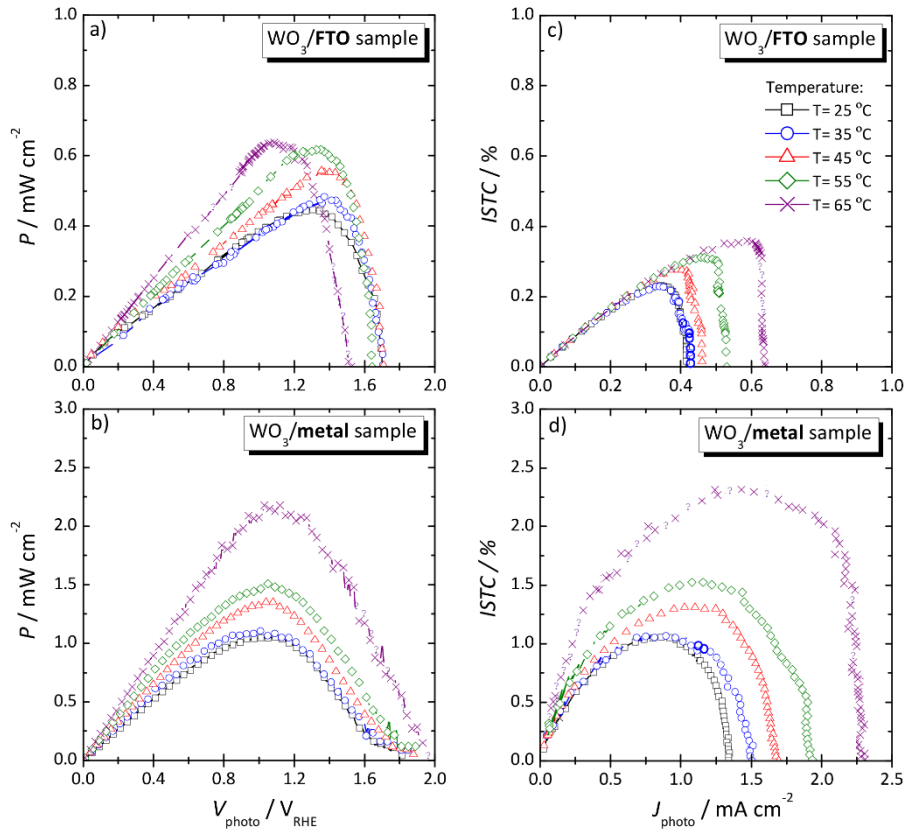


Fig. 7 Temperature effect in the intrinsic power characteristics, *i.e.* the power (P) and intrinsic solar to chemical ($ISTC$) conversion efficiencies, of the WO_3 photoanodes: a) and c) WO_3/FTO sample; and b) and d) WO_3/metal sample. (\square) $T = 25$ °C, (\circ) $T = 35$ °C, (Δ) $T = 45$ °C, (\diamond) $T = 55$ °C, (\times) $T = 65$ °C.

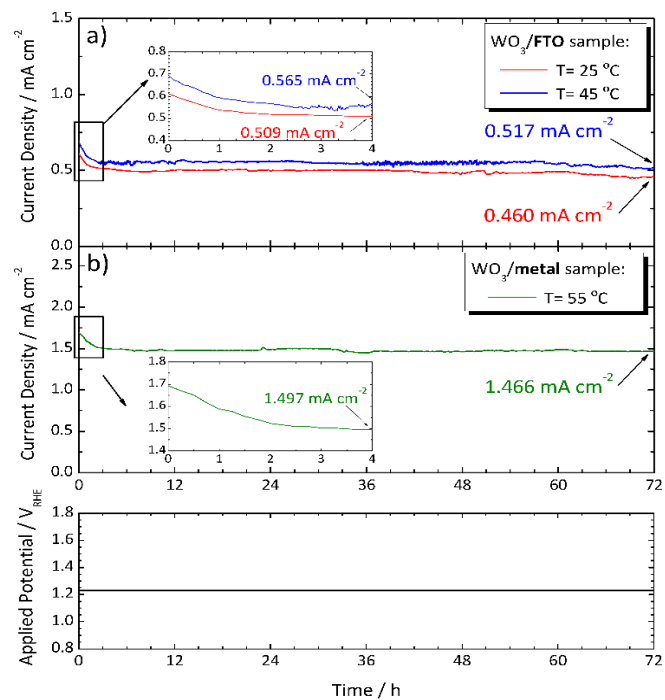


Fig. 8 Photocurrent histories of the WO₃ photoanodes tested over 72 h at a constant potential of *ca.* 1.23 V_{RHE}, under continuous 1 sun AM 1.5 G illumination and at different temperatures: a) WO₃/FTO samples aged at 25 °C (red line) and 45 °C (blue line), and b) WO₃/metal sample aged at 55 °C (green line). Inset plot for the first 4 hours of stability tests.

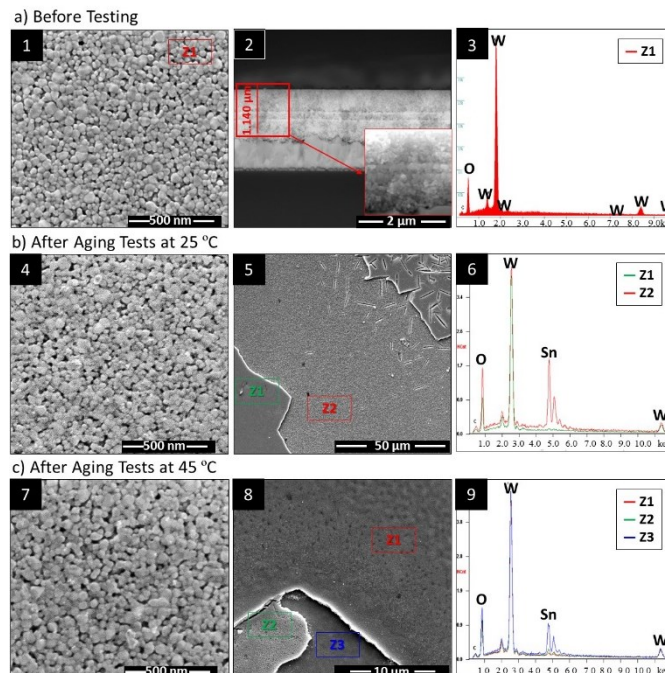


Fig. 9 SEM images of the WO₃/FTO photoanodes. a) Before testing: (1) surface top view; (2) cross sectional view; (3) EDS analysis of the surface with the identification of the tungsten and oxygen peaks; b) After aging tests at 25 °C: (4) surface view; (5) surface with an intact area (Z1) and an area affected by film degradation (Z2); (6) EDS analysis on the two delimited areas with the identification of the tungsten, oxygen and tin peaks; b) After aging tests at 45 °C: (7) surface view; (8) surface with an intact area (Z1) and areas affected by film degradation (Z2 and Z3); (9) EDS analysis on the three delimited zones with the identification of the tungsten, oxygen and tin peaks.

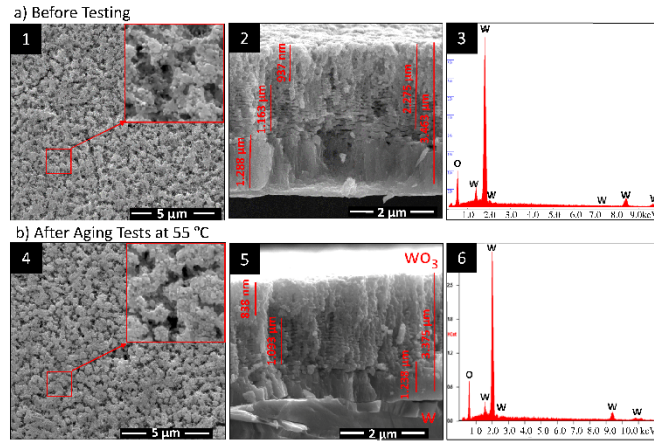


Fig. 10 SEM images of the WO₃/metal photoanodes: (1) and (4) surface top view; (2) and (5) cross sectional view; (3) and (6) EDS analysis with the identification of the tungsten and oxygen peaks; a) before testing and b) after aging tests at 55 °C, respectively.

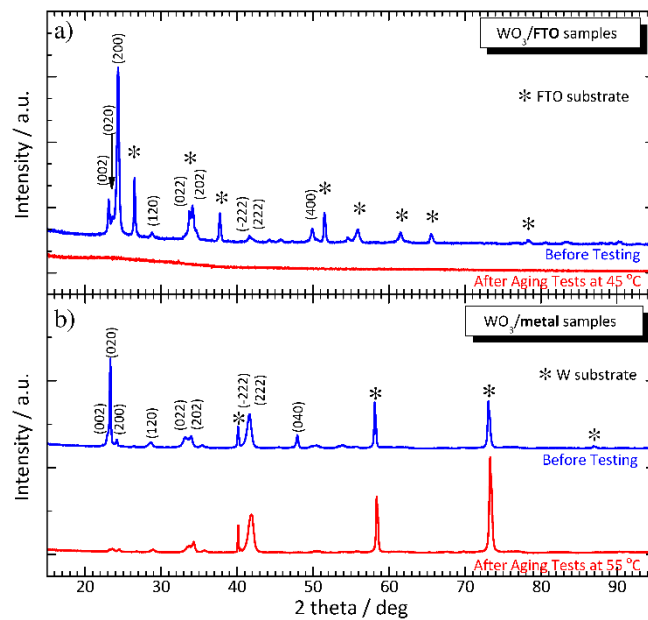


Fig. 11 XRD spectra of the WO₃ photoanodes: a) WO₃/FTO sample aged at 45 °C and b) WO₃/metal sample aged at 55 °C. Blue and red lines correspond to signs of the samples before testing and after aging tests, respectively. Main peaks from the FTO-glass and tungsten substrates are also labeled with “*”.